Real Space Visualization of Competing Phases in $La_{0.6}Sr_{2.4}Mn_2O_7$ Single Crystals

Qiang Zheng,[1,*] Nathaniel J. Schreiber,[3] Hong Zheng,[3] Jiaqiang Yan,[1] Michael A. McGuire,[1] J. F. Mitchell,[3] Miaofang Chi,[2,*] Brian C. Sales[1,*]

[1] Materials Science and Technology Division, Oak Ridge National Laboratory, Oak Ridge, TN 37831, USA

[2] Center for Nanophase Materials Sciences, Oak Ridge National Laboratory, Oak Ridge, TN 37831, USA

[3] Materials Science Division, Argonne National Laboratory, Argonne, IL 60439, USA

[*]Corresponding authors: Q.Z. (zhengq@ornl.gov), M.C. (chim@ornl.gov) and B.C.S. (salesbc@ornl.gov)

ABSTRACT.

Correlated quantum materials are expected to provide the foundation for the next generation of information or energy technologies. A key feature of these materials is the proximity of multiple ground states close in energy, which results in the ability to tune properties with small changes in an external parameter such as magnetic field, composition or temperature. For example the colossal magnetoresistance exhibited by manganites is related to charge and orbital ordering and results from a metallic ferromagnetic phase in proximity to a paramagnetic insulating phase. The presence of competing ground states, at the heart of the physics and functionality of these materials, often results in nanoscale phase separation. Probing nanoscale phase separation with conventional diffraction techniques alone is not adequate, particularly when the domains are small or nanosized. In the present work we use a scanning transmission electron microscopy image-based technique of picometer precision strain maps (PPSM) to directly visualize the competing nanoscale phases with charge and orbital ordering in a double layer manganite. This work underscores the role of subtle structural distortions in determining the electron physics in correlated quantum materials and provides insights into designing new functionalities via spatially tuning multiple competing ground states.

I. INTRODUCTION

In correlated quantum materials involving cations with multiple valence states, the coupling among lattice, charge, orbital and spin degrees of freedom can be tuned to result in the formation of charge and orbital ordering, which can induce various interesting physical phenomena, such as superconductivity and colossal magnetoresistance.[1-4] These correlated quantum materials, such as the colossal magnetoresistance manganites, cuprate and iron-based superconductors, as well as some ferroelectrics, often exhibit nanoscale phase separation, resulting in novel new properties and functionalities. [5-8]The n = 2 Ruddlesden-Popper phase $La_{2-2x}Sr_{1+2x}Mn_2O_7$ (LSMO) represents one of such cases in which charge and orbital ordering can be tuned by varying x. Specifically, when x is below 0.66 or above 0.74, this material exhibits clearly different long-range magnetic orders due to different charge/orbital ordering patterns in the lattice. However, in the phase diagram,[9-10] no long-range magnetic order was found using neutron powder diffraction for $0.66 \leq x \leq 0.74$ but nanoscale phase competition was suggested by the neutron pair distribution function (PDF) technique. Recently, a large single crystal with x = 0.7 (LSMO-0.7), located in this region, has been grown using the floating-zone method under high oxygen pressure and exhibits complex long-range magnetic order. These seemingly contradictory results indicate a complex interplay and competition between different degrees of freedom in this crystal, which however is difficult to understand using bulk diffraction techniques, such x-ray and neutron diffraction.[9, 11] While conventional transmission electron microscopy (TEM) imaging and diffraction are often used to study local charge or orbital ordering via their induced structural modulations,[12-13] they are either limited in high-spatial resolution or complicated by the interpretation of phase contrast and reciprocal space behaviors. Recently developed scanning transmission electron microscopy (STEM) image-based picometer-precision measurements on

cationic column positions[14-16] and sub-Å spatial resolution spectroscopy[17-18] provide a possible effective way to probe into such nanoscale complexity and the competition between different degrees of freedom in this LSMO-0.7 crystal. Especially, the local orbital ordering in $La_{2-2x}Sr_{1+2x}Mn_2O_7$ (LSMO) structures only produces tiny differences between elongated and compressive Mn-O bond lengths.[19] These differences are too small to be detected by measuring the oxygen positions from annular bright field-STEM (ABF) images, but charge and orbital behaviors can be inferred from the local cationic lattice response in such structures.

In the present work we illustrate the power of the STEM image-based technique of picometer precision strain maps (PPSM) of the cationic lattice to both visualize and characterize phase separation and charge and orbital ordering in such correlated quantum materials. We use atomic scale aberration-corrected STEM imaging and electron energy loss spectroscopy (EELS) as well as AC and DC magnetic susceptibility, electrical transport, and heat capacity measurements to characterize the $La_{0.6}Sr_{2.4}Mn_2O_7$ crystals. We find that the crystals are phase separated at the nanoscale with La rich and La poor domains corresponding to $x \approx 0.67$ and $x \approx 0.74$ respectively, resulting in an average composition of $x \approx 0.7$. The typical domain size is 10-15 nm. The orbital patterns in each type of domain are inferred from PPSM determined from precise picometer-level measurements of atom positions of STEM images, combined with single column EELS mapping of the distribution of the different oxidation states. Charge ordering stripes of Mn^{3+} and Mn^{4+} are deduced to be spatially correlated with periodic picometer level shear deformations via cooperative Jahn-Teller distortion associated with in-plane $d_{3x^2-r^2}$ and $d_{3y^2-r^2}$ orbital ordering in Mn^{3+} stripes. This work not only elucidates the complex interplay and competition between different degrees of freedom in a manganite, but also highlights the importance of subtle

structural distortions in determining the electron physics and functionalities in correlated quantum materials.

II. EXPERIMENTAL SECTION

Materials preparation. A single crystal of $La_{2-2x}Sr_{1+2x}Mn_2O_7$ (x = 0.7) was prepared by a floating zone technique in an NEC two-mirror image furnace. Polycrystalline feed rods were prepared by solid state reaction. Growth occurred in an atmosphere of pure oxygen and a gauge pressure of 9 bar. Single crystals of size suitable for the measurements described here were cleaved from the boule.

Physical property measurements. Temperature-dependent DC and AC magnetic measurements were performed on the $La_{2-2x}Sr_{1+2x}Mn_2O_7$ (x = 0.7) crystal using a Magnetic Property Measurement System (MPMS, Quantum Design) and the AC susceptibility option of a Physical Property Measurement System (PPMS, Quantum Design), respectively, in zero-field-cooled or field-cooled modes, with field perpendicular to or parallel to the *ab*-plane. Temperature-dependent electrical resistivity (ρ) and heat capacity (c_p) data were collected using a PPMS.

STEM imaging and spectroscopy. Scanning transmission electron microscopy (STEM) specimens were prepared by crushing a small single crystal in ethanol. Drops of the resulting suspensions were deposited on lacey carbon TEM grids, and then dried in air. High-angle annular dark-field (HAADF) imaging and electron-energy loss spectroscopy (EELS) were performed on a Nion UltraSTEM100,[20] equipped with a cold field-emission electron source and a corrector of third and fifth-order aberrations, operated at an accelerating voltage of 100 kV.

HAADF-STEM images were collected with a probe convergence angle of 30 mrad and an inner collection angle of 86 mrad. EEL spectra were collected using a Gatan Enfinium spectrometer (Gatan Inc.), with a dispersion of 0.3~0.5 eV per channel and collection semi-angle of 48 mrad. The specimens were held in the microscope chamber until the stages were stable before imaging and spectrum acquisition. Each HAADF image was collected by stacking 20 fast scanned images (1~2 μs/pixel dwell time). Before summing, the images were aligned using phase correlation to reduce drift between subsequent images. A dwell time of 0.1 s per pixel was used to increase the signal-to-noise ratio in the spectrum images. 2D displacement maps (PPSM) and the GPA method were used to analyze strain fields present in HAADF-STEM images using a MatLab code in StatSTEM software[21] and plugins of GPA within Gatan DigitalMicrograph software,[22] respectively. Electron diffraction was carried out on a field-emission FEI Tecnai G2 F20 at 200 kV.

III. RESULTS AND DISCUSSION

Competing nanoscale phases with varying La contents. $La_{2-2x}Sr_{1+2x}Mn_2O_7$ (LSMO) ideally has a tetragonal structure (*I*4/*mmm*) that is comprised of two identical slabs stacked along the *c* axis, with each slab shifted by $^1/_2(\boldsymbol{a} + \boldsymbol{b} + \boldsymbol{c})$ with respect to the other. The slabs contain two perovskite (P)-like (La, Sr)MnO_3 layers and one rock-salt (RS)-like (La, Sr)O layer. In the LSMO (x = 0.7, LSMO-0.7) structure, Sr^{2+} preferentially occupies cation sites in the RS-layer, while La^{3+} favors the P-layer, similar to that previously observed in LSMO single crystals with x = 0.36, 0.5 and 0.56.[23] For the LSMO-0.7 crystals investigated in the present work, measurements of magnetic susceptibility, electrical resistivity and heat capacity all show anomalies at 320-330K, consistent

with the occurrence of charge and orbital ordering at this temperature. See more detail in Supporting Text 1-3, and Figures S1-S5. Therefore, the STEM experiment carried out at room temperature (293 K), at which this LSMO-0.7 single crystal shows charge and orbital ordering behaviors, could well reveal the local structural responses due to such ordering.

As shown in Figure 1a, a typical high angle annular dark field (HAADF)-STEM image along [001] for the LSMO-0.7 single crystal reveals such crystal is seemingly structurally perfect. However, its fast Fourier transform (FFT) pattern given in Figure 1b reveals two sets of satellite spots $\boldsymbol{G}\pm\boldsymbol{q}_1$ and $\boldsymbol{G}\pm\boldsymbol{q}_2$ in addition to strong Bragg reflections G, arising from periodic structural modulations (satellite spots with modulated vector $\boldsymbol{q}_1$ and $\boldsymbol{q}_2$ surrounding (000) and (020) are arrowed in green and red, respectively). Figure 1c displays typical selected-area electron diffraction (SAED) pattern for a region with size of ~200 nm, showing similar satellite spots surrounding the main reflections. Meanwhile, obvious splitting of these satellite spots in this SAED pattern indicates two modulations of different wavelength and phase separation in the crystal. To visualize the structural modulations, a mask was applied to block all the spots except these satellites and then an inverse FFT was performed. Applying this processing, the inverse FFT pattern of Figure 1b is depicted in Figure 1d, clearly illustrating the interpenetrating structural modulations in real space. Two different types of nanoscale domains are found, as exemplified by black and red dashed-line rectangles, respectively, indicating two competing nanoscale phases in this crystal. The former one consists of stripes with unidirectional structural modulation, while the latter one is formed by 90° stripe domains with bidirectional modulations. The periodicity of the modulation for the former one is longer than that of the latter one, as analyzed later in Figure 2 and Figure 3, respectively. While many previous studies revealed that such structural modulations in perovskite and related structures are related to charge and orbital

ordering,[4, 24-26] real-space experiments that clearly demonstrate their microscopic origin and features are quite lacking.

Moreover, these two types of domains show not only structural differences but also slightly different La/Sr ratios. The EELS spectra for the two regions are shown in Figure 1e. The 90° domain region contains more La and correspondingly involves a lower average Mn oxidation state as indicated by the chemical shift of its Mn *L*-edge towards lower energy.[17, 27-28] Although the La/Mn ratios in the two phases differ by round 20%, because the crystals contains much more Sr than La and the effects of probe channeling,[29] there is no obvious intensity enhancement in the HAADF images for the phase with larger La/Mn ratio. This is consistent with the calculated change in intensity enhancement, which was estimated to be less than 3%. Nevertheless, these data further indicate the nanoscale coexistence and competition of two chemically and structurally distinct modulated phases in this LSMO-0.7 single crystal. In what follows, we will provide real space information about these two types of domains, and provide insight into their microscopic origins.

Picometer precision strain maps (PPSM). Figure 2a shows a [001] HAADF-STEM image of the domain with a unidirectional structural modulation. Its FFT pattern (Figure S7a) reveals only one set of satellite spots $\boldsymbol{G} \pm \boldsymbol{q}_1$ in addition to strong Bragg reflections $\boldsymbol{G}$ (the pair surrounding (110) are arrowed in green in the inset of Figure 2a), where $\boldsymbol{q}_1$ is $0.131[1\bar{1}0]^*$. However, this structural modulation is not readily obvious from the HAADF image in Figure 2a. Using a mask mentioned above (Figure S7b) and an inverse FFT processing (Figure S7c), the structural modulation could be clearly represented with a periodicity of $L = 7\sim8d_{(1\text{-}10)}$, *i.e.* 20.3 ±1.4 Å in real space.

This structural modulation is attributed to periodic tiny lattice distortions, and real-space local strain analysis on HAADF images could evidently visualize such tiny structural distortion. The refined atomic positions of each column of atoms in Figure 2a is first determined with picometer accuracy using 2D Gaussian fitting (see Supporting Text 4 for more details)[21, 30] Using the refined atomic positions, PPSM were determined from an analysis of Figure 2a, as presented in Figure 2b-d. Figure 2b, c displays ε_{xx} and ε_{yy} component, *i.e.* the uniaxial deformation along *x* ([100]) and *y* ([010]), respectively. ε_{xx} and ε_{yy} both show alternating positive and negative stripes along $[1\,\bar{1}\,0]$ with a periodicity of 7~8 layers, consistent with the structural modulation determined above. The tiny shear component ε_{xy} and obvious rotation component ω_{xy} (Figure 2d) indicate a rigid rotation of the lattice between -1.15° to 1.15°. The geometric phase analysis (GPA) method (see Supporting Text 5 for more details)[31] was also applied to this image, resulting in the same strain maps (Figure S8). To visualize the lattice distortion, a schematic of the deformation for a unit cell (small dashed-line square region in Figure 2d) with $\varepsilon_{xx} > 0$, $\varepsilon_{yy} < 0$ and $\omega_{xy} > 0$ is demonstrated in Figure 2e. The resultant total strain could thus be described by the simple transverse shear strain along $[\bar{1}\bar{1}0]$, as clearly revealed by the deformation of a primitive cell. The blue solid-line and red dashed-line lozenge in Figure 2e defines a primitive cell before and after deformation, respectively. In comparison, in the regions with reverse strains, *i.e.* $\varepsilon_{xx} < 0$, $\varepsilon_{yy} > 0$ and $\omega_{xy} < 0$, the resultant total strain is simple shear along [110] with a 180° reversal. This local strain also reduces the crystal symmetry from tetragonal to orthorhombic.

To further evaluate the strain variation along the modulation direction $[1\bar{1}0]$, we define two inner angles α and β and the lengths of diagonal lines d_x and d_y of the primitive-cell lozenges along this direction, as presented in Figure 2f. The image enclosed by the rectangular black solid line in

Figure 2d was used for averaging and analysis. Figure 2g shows the resulting image analysis, indicating that α and β periodically oscillate in the range of 89 to 92° and d_x and d_y change in the range of 376 to 388 pm with the same periodicity. It also emerges that the values of α and β vary in an opposite way as well as d_x and d_y. The 180° strain reversal between two neighboring stripes is also demonstrated by α and β above or below 90°, and d_x and d_y longer or shorter than 381 pm. To obviously visualize the boundary of this 180° strain reversal, we also plotted the sum of β_i and α_{i+1} for two neighboring lozenges in Figure 2g. The maxima and minima both designate the occurrence of 180° strain reversal, and simple shear along the same direction is colored identically in Figure 2g, in good agreement with the strain maps presented in Figure 2b-d.

PPSM for the HAADF images of 90° stripe domains could also be obtained using quantitative real-space strain analysis. Figure 3a displays a [001] HAADF-STEM image of 90° stripe domains with bidirectional modulations. Figure S8a shows its FFT pattern, signifying two structural modulations with 90° alternation of orientations. Modulation vectors $\boldsymbol{q}_1$ and $\boldsymbol{q}_2$ of these two sets of satellite reflections (ones of which surrounding main reflection (110) and $(\bar{1}10)$ are arrowed in green and red, respectively) are $0.157[1\bar{1}0]^*$ and $0.157[110]^*$, respectively. The lengths of these modulation vectors are longer than those in Figure 2a, *i.e.* modulation periodicity L in real space becomes shorter from 7~8 $d_{(1\text{-}10)}$ to 6~7 $d_{(1\text{-}10)}$ (17.6 ±1.4 Å). This variation of periodicity is due to varying La/Sr contents in these two types of domains, as revealed by EEL spectra in Figure 1e. The real-space PPSM for this HAADF image are presented in Figure 3b-d. GPA analysis for the strain fields are given in Figure S10. The strain maps from both methods indicate that lattices of these regions undergo bidirectional transverse shear strains, causing different ground state as comparison to the region in Figure 2. The local PPSM for such 90° stripe domains suggests the symmetry is on average tetragonal. Moreover, it

is worth pointing out that, since these two types of domains are ~10nm in size, superposition along the electron beam direction of two unidirectional domains in 90° rotation can sometimes be observed, which show similar patterns with the 90° stripe domains in Figure 3. However, since the La content and the periodicity of modulation for such superposition are not the same as those for the 90° stripe domains, it is easy to distinguish the 90° stripe domains from such superposition.

From previous work it is known that $^1/_r$ in the modulation propagation vector $\boldsymbol{q} = {}^1/_r[1\bar{1}0]^*$ (or $^1/_r[110]^*$) is roughly linear in x in $La_{2-2x}Sr_{1+2x}Mn_2O_7$, *e.g.* $^1/_r = {}^1/_6$, $^1/_7$, and $^1/_8$ for x = 0.66, 0.71, and 0.75, respectively.[24-25, 32] Therefore, $^1/_r$ = 0.131 for the modulation vectors in Figure 2a and 0.157 in Figure 3a correspond to $x \approx 0.74$ and 0.67, respectively, both only slightly different from the nominal composition x = 0.7. However, this small composition variation leads to the local nanoscale competition between ordered ground states found in two different regions of the phase diagram.[9-10] The average Mn oxidation states for the two phases with x = 0.74 and 0.67 are +3.74 and +3.67, while La/Mn atomic ratios are 0.26 and 0.33, respectively. This explains the slight difference between Mn *L*-edges while obvious difference between La *M*-edges in their EEL spectra in Figure 1e. These two regions were proposed to be associated with $d_{y^2-3r^2}$ orbital order and an orthorhombic structure, and $d_{x^2-y^2}$ orbital order and a tetragonal structure, respectively. More than ten different regions were randomly selected from this large LSMO-0.7 single crystal, and all reveal similar feature as shown in Figure 1, indicating such phase competition is universal across the whole crystal. The volume contents for the two types of regions are also comparable. The coexistence of two nanophases revealed here is consistent with the proposed models of Qiu *et al.*,[33] *i.e.*, a mixed, short-range ordered magnetic ground state attached to nano-scale orbital ordered regions. However, the complex interplay and competition

between these two phases might lead to a novel magnetic ground state and functionality different from that expected for each region. This has been well illustrated in the case of $TlFe_{1.6}Se_2$ where the interaction and coupling between the regions with ordered and disordered Fe vacancies result in a new ground state.[34] It could be reasonably speculated that such novel magnetic ground state and functionality vary and are dominated by contents of the two competing phases, *i.e.* nominal *x* for the crystal. Slight adjustment of *x* in the range of 0.66 and 0.74 may result in many complex interplays and competitions between these two phases and different functionalities.

Charge ordering stripes of Mn^{3+} and Mn^{4+}. The structural modulations in LSMO are related to local charge and/or orbital ordering stripes, while the correlation between them is often overlooked using conventional diffraction techniques, especially for cases with coherence lengths short to nanoscale.[9, 19, 24-25, 35-37] Here image-based PRSM, associated with structural modulations, are most likely attributed to the local coupling between lattice distortions and charge/orbital ordering. To further verify the correlation between the PPSM and Mn oxidation state distribution, high-spatial resolution EELS-STEM analysis were carried out, where the $L_{2,3}$ ratio is used to estimate the oxidation state of 3*d* transition metals (See Supporting Text 6 for more details).[17, 27-28] A schematic of the EELS experiments are shown in Figure 4a. EELS scans are performed along the [001] direction (Figure 4c) and the $[1\bar{1}0]$ direction (Figure 4d) which are both in the (110) plane. Mn^{3+} ions reside in pink O octahedra while Mn^{4+} ions are in blue O octahedra.

We first acquired atomic-resolution EELS data set along [001] zone axis at thin regions ($< 0.3\lambda$, where λ is electron mean free path for inelastic scattering in this crystal), such as the one

shown in Figure 4c. To avoid the 90° domain regions and simplify the analysis, the selected region only contained unidirectional structural modulation, as proved by a strain map in the left panel of Figure 4c. Mn $L_{2,3}$ ratios could be acquired for all the atomic columns containing Mn in this region, and Figure 4b displays two typical spectra from atomic column containing Mn cations with more reduced and more oxidized states, respectively. As compared to Mn with more oxidized states, Mn with more reduced states has a larger $L_{2,3}$ ratio and the chemical shift towards low energy. The Mn $L_{2,3}$ ratios for all the atomic columns in this region are plotted in the right panel of Figure 4c. Nearly all error bars are lower than 5 %, which were estimated from the errors introduced in background subtraction and noise in the data.[17, 27] It is obvious that Mn $L_{2,3}$ ratios are distributed around 2.1 and 2.7, corresponding to the oxidation states close to Mn^{4+} and Mn^{3+}, respectively.[17] The discrepancy of $L_{2,3}$ ratios between the columns with same Mn oxidation states is resulted from the intermixing of the inelastic signal due to probe delocalizing and elastic scattering,[38] and often appears in atomic-level EEL spectra.[18] Such intermixing can cause a fraction of Mn^{4+} signal to be measured at Mn^{3+} columns and vice versa. Moreover, since the total number of Mn^{4+} ions is twice of the Mn^{3+} ions in this LSMO-0.7 crystal, the discrepancy is larger for Mn^{3+} than that for Mn^{4+}. Nevertheless, Figure 4c obviously reveals that all Mn cations charge equivalently in each (110) plane, forming charge ordered stripes in the (110) plane (see the structure schematic in Figure 4a and Figure S12a), strongly correlated with PPSM.

To further confirm such charge ordering stripes in the (110) planes, we also analyzed the Mn oxidation state distribution in the $[1\bar{1}0]$ projection, which is rotated 90° in the (110) plane relative to [001]. As shown in Figure 4d, the simultaneously obtained chemical maps for the La $M_{4,5}$-edges and Mn $L_{2,3}$-edges are displayed in the left panel of Figure 4d. In the projection along

this zone axis, two alternating perovskite slabs are quite easy to distinguish. Consistent with $L_{2,3}$ ratio analysis along [001] in Figure 4c, analysis along [$1\bar{1}0$] verifies the formation of charge ordering stripes in the (110) plane (Figure 4a and Figure S12b) and strong correlation between charge ordering pattern and image-based PPSM in this LSMO-0.7 single crystal.

Since the atomic displacements in manganites principally associate with a large lattice response to the Jahn-Teller distortion of Mn^{3+} ($3d^4$),[4, 19, 24] the strong correlation between charge ordering pattern and image-based PPSM here arise likely from orbital ordering, and the orbital ordering pattern in the charge ordered stripes can be inferred from the periodic distributions of the strain field. Figure 5 shows a deduced orbital ordering pattern with a periodicity of $6d_{(110)}$ for the phase with unidirectional structural modulation in LSMO-0.7. In this pattern, due to $d_{3x^2-r^2}$ or $d_{3y^2-r^2}$ orbital ordering in each Mn^{3+} stripe, the oxygen octahedra are compressed along *y* (or *x*) while elongated along *x* (or *y*), causing their surrounding cations to move towards the same directions, *i.e.* a simple-shear transverse lattice deformation. The local strain field that is generated is displayed at the top of Figure 5. 180° strain reversals occur at two Mn^{4+} stripes between two Mn^{3+} stripes in each periodicity due to the alternation of lattice displacement directions. The chemical composition, or the $Mn^{3+/}Mn^{4+}$ ratio, determines the periodicity or the separation between charge/orbital ordered stripes.

IV. CONCLUSIONS

In summary, the quantitative sub-Å STEM imaging and spectroscopy study presented in this work elucidates the correlations among lattice, charge and orbital degrees of freedom in a layered LSMO-0.7 single crystal. We have used atomic-resolution HAADF imaging to visualize the phase separation and probe the local periodic strain field associated with subtle cationic

displacements at the picometer-level using PPSM. Using EELS $L_{2,3}$ ratio method, we are able to analyze the local Mn oxidation states and depict the charge ordering stripes of Mn^{3+} and Mn^{4+}, which strongly correlate with PPSM. Such strong correlation between the charge ordering stripes and local periodic strain fields is inferred to be due to local Jahn-Teller distortion accompanied by the cooperative displacements. The orbital ordering pattern in the charge ordered stripes has been proposed from the periodic distributions of the strain field. Our PPSM analyses also directly evidence the appearance of two types of nanoscale phases in LSMO-0.7 single crystal. The chemical and structural difference between them leading to nanoscale competition and interaction between different short-range ground states accounts for the bulk properties of LSMO with x in the range of 0.66~0.74 indicating a possibility to design new functionalities via introducing and tuning multiple competing ground states in correlated quantum materials. This real space atomic-scale imaging study also open a pathway for future investigations on interplay among lattice, charge and orbital degrees of freedom and local cooperative Jahn-Teller distortions and induced strain fields in complex correlated quantum materials.

ACKNOWLEDGMENT

Work in the Materials Science and Technology Division at Oak Ridge National Laboratory (magnetic, transport, thermodynamic and microscopy characterization) and in the Materials Science Division of Argonne National Laboratory (single crystal growth and magnetic characterization) was supported by the U.S. Department of Energy (DOE), Office of Science, Basic Energy Sciences (BES), Materials Sciences and Engineering Division. The microscopy in

this work was conducted at the ORNL's Center for Nanophase Materials Sciences (CNMS), which is a DOE Office of Science User Facility.

ASSOCIATED CONTENT

Supporting Information. Supporting Information including Supporting Texts (crystal structure; atomic-level EELS mapping; physical properties; Real-space peak pairs analysis; geometric phase analysis and $L_{2,3}$ ratio method from EEL spectra) and Supplementary Figures (crystal structure; atomic-level EELS maps along [110], [100] and [001]; physical properties including transport properties and DC and AC susceptibilities; superstructure analysis; FFT and inverse FFT patterns; GPA analysis; $L_{2,3}$ ratio method from EEL spectra; schematic of Mn^{3+} and Mn^{4+} distribution).

The Supporting Information is available free of charge on the ACS Publications website.

AUTHOR INFORMATION

Corresponding Author

* Q.Z. (zhengq@ornl.gov), M.C. (email: chim@ornl.gov) and B.C.S. (salesbc@ornl.gov)

Notes

The authors declare no competing financial interest.

REFERENCES

1. Rao, C. N. R.; Raveau, B., *Colossal magnetoresistance, charge ordering and related properties of manganese oxides*. World Scientific: 1998.
2. da Silva Neto, E. H.; Aynajian, P.; Frano, A.; Comin, R.; Schierle, E.; Weschke, E.; Gyenis, A.; Wen, J.; Schneeloch, J.; Xu, Z., Ubiquitous interplay between charge ordering and high-temperature superconductivity in cuprates. *Science* **2013**, 1243479.
3. Moritomo, Y.; Asamitsu, A.; Kuwahara, H.; Tokura, Y., Giant magnetoresistance of manganese oxides with a layered perovskite structure. *Nature* **1996,** *380*, 141−144.
4. Tokura, Y.; Nagaosa, N., Orbital Physics in Transition-Metal Oxides. *Science* **2000,** *288*, 462−468.
5. Dagotto, E.; Hotta, T.; Moreo, A., Colossal magnetoresistant materials: the key role of phase separation. *Phys. Rep.* **2001,** *344*, 1−153.
6. Dagotto, E., Correlated electrons in high-temperature superconductors. *Rev. Mod. Phys.* **1994,** *66*, 763−840.
7. Emery, V. J.; Kivelson, S. A., Frustrated electronic phase separation and high-temperature superconductors. *Physica C* **1993,** *209*, 597−621.
8. Lunkenheimer, P.; Krohns, S.; Riegg, S.; Ebbinghaus, S. G.; Reller, A.; Loidl, A., Colossal dielectric constants in transition-metal oxides. *Eur. Phys. J.: Spec. Top.* **2009,** *180*, 61-89.
9. Ling, C. D.; Millburn, J. E.; Mitchell, J. F.; Argyriou, D. N.; Linton, J.; Bordallo, H. N., Interplay of spin and orbital ordering in the layered colossal magnetoresistance manganite $La_{2-2x}Sr_{1+2x}Mn_2O_7$ ($0.5 \leq x \leq 1.0$). *Phys. Rev. B* **2000,** *62*, 15096−15111.
10. Mitchell, J. F.; Ling, C. D.; Millburn, J. E.; Argyriou, D. N.; Berger, A.; Medarde, M., Magnetic phase diagram of layered manganites in the highly doped regime. *J. Appl. Phys.* **2001,** *89*, 6618−6620.
11. Joonghoe, D.; Kim, W. S.; Choi, H. S.; Chi, E. O.; Hur, N. H., Re-entrant charge-ordering behaviour in the layered manganites $La_{2-2x}Sr_{1+2x}Mn_2O_7$. *J. Phys. Condens. Matter* **2001,** *13*, 3655.
12. Tao, J.; Niebieskikwiat, D.; Varela, M.; Luo, W.; Schofield, M. A.; Zhu, Y.; Salamon, M. B.; Zuo, J. M.; Pantelides, S. T.; Pennycook, S. J., Direct Imaging of Nanoscale Phase Separation in $La_{0.55}Ca_{0.45}MnO_3$: Relationship to Colossal Magnetoresistance. *Phys. Rev. Lett.* **2009,** *103*, 097202.
13. Mori, S.; Chen, C. H.; Cheong, S. W., Pairing of charge-ordered stripes in $(La,Ca)MnO_3$. *Nature* **1998,** *392*, 473.
14. Savitzky, B. H.; El Baggari, I.; Admasu, A. S.; Kim, J.; Cheong, S.-W.; Hovden, R.; Kourkoutis, L. F., Bending and breaking of stripes in a charge ordered manganite. *Nat. Commun.* **2017,** *8*, 1883.
15. Yankovich, A. B.; Berkels, B.; Dahmen, W.; Binev, P.; Sanchez, S. I.; Bradley, S. A.; Li, A.; Szlufarska, I.; Voyles, P. M., Picometre-precision analysis of scanning transmission electron microscopy images of platinum nanocatalysts. *Nat. Commun.* **2014,** *5*, 4155.
16. El Baggari, I.; Savitzky, B. H.; Admasu, A. S.; Kim, J.; Cheong, S.-W.; Hovden, R.; Kourkoutis, L. F., Nature and evolution of incommensurate charge order in manganites visualized with cryogenic scanning transmission electron microscopy. *Proc. Natl. Acad. Sci. U. S. A.* **2018**, *115*, 1445−1450.

17. Varela, M.; Oxley, M. P.; Luo, W.; Tao, J.; Watanabe, M.; Lupini, A. R.; Pantelides, S. T.; Pennycook, S. J., Atomic-resolution imaging of oxidation states in manganites. *Phys. Rev. B* **2009,** *79*, 085117.
18. Tan, H.; Turner, S.; Yücelen, E.; Verbeeck, J.; Van Tendeloo, G., 2D Atomic Mapping of Oxidation States in Transition Metal Oxides by Scanning Transmission Electron Microscopy and Electron Energy-Loss Spectroscopy. *Phys. Rev. Lett.* **2011,** *107*, 107602.
19. Argyriou, D. N.; Bordallo, H. N.; Campbell, B. J.; Cheetham, A. K.; Cox, D. E.; Gardner, J. S.; Hanif, K.; dos Santos, A.; Strouse, G. F., Charge ordering and phase competition in the layered perovskite $LaSr_2Mn_2O_7$. *Phys. Rev. B* **2000,** *61*, 15269−15276.
20. Krivanek, O. L.; Corbin, G. J.; Dellby, N.; Elston, B. F.; Keyse, R. J.; Murfitt, M. F.; Own, C. S.; Szilagyi, Z. S.; Woodruff, J. W., An electron microscope for the aberration-corrected era. *Ultramicroscopy* **2008,** *108*, 179−195.
21. De Backer, A.; van den Bos, K. H. W.; Van den Broek, W.; Sijbers, J.; Van Aert, S., StatSTEM: An efficient approach for accurate and precise model-based quantification of atomic resolution electron microscopy images. *Ultramicroscopy* **2016,** *171*, 104−116.
22. Koch, C. Determination of Core Structure Periodicity and Point Defect Density along Dislocations. Arizona State University, 2002.
23. Roldan, M. A.; Oxley, M. P.; Li, Q. a.; Zheng, H.; Gray, K. E.; Mitchell, J. F.; Pennycook, S. J.; Varela, M., Atomic Scale Studies of La/Sr Ordering in Colossal Magnetoresistant $La_{2-2x}Sr_{1+2x}Mn_2O_7$ Single Crystals. *Microsc. Microanal.* **2014,** *20*, 1791−1797.
24. Luo, Z. P.; Miller, D. J.; Mitchell, J. F., Electron microscopic evidence of charge-ordered bi-stripe structures in the bilayered colossal magnetoresistive manganite $La_{2-2x}Sr_{1+2x}Mn_2O_7$. *Phys. Rev. B* **2005,** *71*, 014418.
25. Li, J. Q.; Dong, C.; Liu, L. H.; Ni, Y. M., Reentrant charge-ordering transition and phase separation in the layered perovskite $La_{2-2x}Sr_{1+2x}Mn_2O_7$. *Phys. Rev. B* **2001,** *64*, 174413.
26. Chen, C. H.; Cheong, S. W., Commensurate to Incommensurate Charge Ordering and Its Real-Space Images in $La_{0.5}Ca_{0.5}MnO_3$. *Phys. Rev. Lett.* **1996,** *76*, 4042−4045.
27. Wang, Z. L.; Bentley, J.; Evans, N. D., Valence state mapping of cobalt and manganese using near-edge fine structures. *Micron* **2000,** *31*, 355−362.
28. Tan, H.; Verbeeck, J.; Abakumov, A.; Van Tendeloo, G., Oxidation state and chemical shift investigation in transition metal oxides by EELS. *Ultramicroscopy* **2012,** *116*, 24−33.
29. Esser, B. D.; Hauser, A. J.; Williams, R. E. A.; Allen, L. J.; Woodward, P. M.; Yang, F. Y.; McComb, D. W., Quantitative STEM Imaging of Order-Disorder Phenomena in Double Perovskite Thin Films. *Phys. Rev. Lett.* **2016,** *117*, 176101.
30. Galindo, P. L.; Kret, S.; Sanchez, A. M.; Laval, J.-Y.; Yáñez, A.; Pizarro, J.; Guerrero, E.; Ben, T.; Molina, S. I., The Peak Pairs algorithm for strain mapping from HRTEM images. *Ultramicroscopy* **2007,** *107*, 1186−1193.
31. Hÿtch, M. J.; Snoeck, E.; Kilaas, R., Quantitative measurement of displacement and strain fields from HREM micrographs. *Ultramicroscopy* **1998,** *74*, 131−146.
32. Li, J. Q.; Matsui, Y.; Kimura, T.; Tokura, Y., Structural properties and charge-ordering transition in $LaSr_2Mn_2O_7$. *Phys. Rev. B* **1998,** *57*, R3205−R3208.
33. Qiu, X.; Billinge, S. J. L.; Kmety, C. R.; Mitchell, J. F., Evidence for nano-scale inhomogeneities in bilayer manganites in the Mn^{4+} rich region: $0.54 \leq x \leq 0.80$. *J. Phys. Chem. Solids* **2004,** *65*, 1423−1429.

34. May, A. F.; McGuire, M. A.; Cao, H.; Sergueev, I.; Cantoni, C.; Chakoumakos, B. C.; Parker, D. S.; Sales, B. C., Spin Reorientation in $TlFe_{1.6}Se_2$ with Complete Vacancy Ordering. *Phys. Rev. Lett.* **2012,** *109*, 077003.
35. Beale, T. A. W.; Spencer, P. D.; Hatton, P. D.; Wilkins, S. B.; Zimmermann, M. v.; Brown, S. D.; Prabhakaran, D.; Boothroyd, A. T., Orbital bi-stripes in highly doped bilayer manganites. *Phys. Rev. B* **2005,** *72*, 064432.
36. Beale, T. A. W.; Bland, S. R.; Hatton, P. D.; Thompson, P.; Prabhakaran, D.; Boothroyd, A. T., X-ray resonant scattering study of the incommensurate charge-orbital density wave $La_{2-2x}Sr_{1+2x}Mn_2O_7$ (x = 0.7). *J. Phys: Conf. Ser.* **2010,** *211*, 012006.
37. Sun, Z.; Wang, Q.; Fedorov, A. V.; Zheng, H.; Mitchell, J. F.; Dessau, D. S., Localization of electrons due to orbitally ordered bi-stripes in the bilayer manganite $La_{2-2x}Sr_{1+2x}Mn_2O_7$ (x~0.59). *Proc. Natl. Acad. Sci. U. S. A.* **2011,** *108*, 11799−11803.
38. Verbeeck, J.; Schattschneider, P.; Rosenauer, A., Image simulation of high resolution energy filtered TEM images. *Ultramicroscopy* **2009,** *109*, 350−360.

Figures and captions

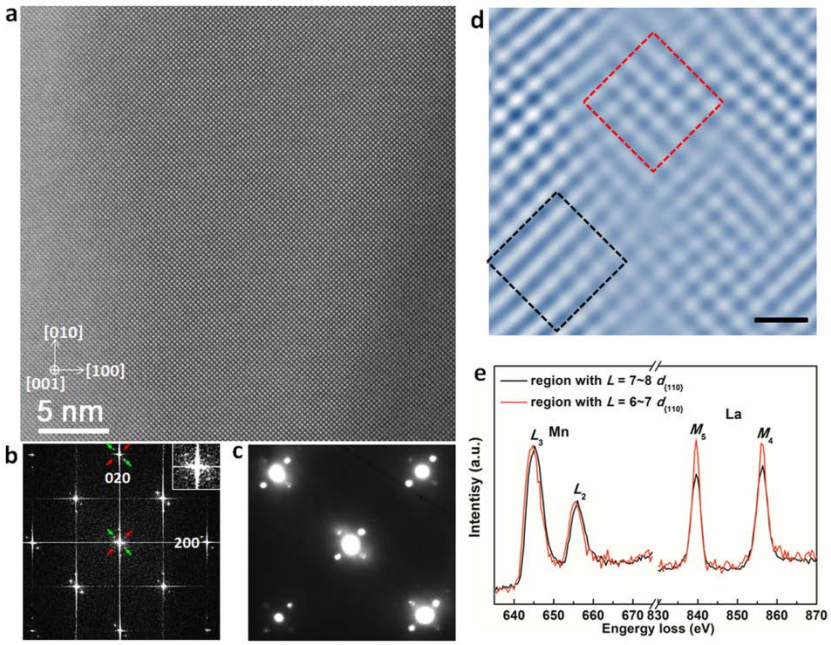

Figure 1. Local competing and interpenetrating nanoscale domains with varying La contents in LSMO-0.7 single crystal. (a) A typical atomic-resolution HAADF-STEM image along the [001] zone axis. (b) Fast Fourier transform (FFT) pattern of (a) reveals appearance of structural modulations in this crystal. Two sets of satellite spots neighboring (000) and (020), corresponding to structural modulations along [110] and $[1\bar{1}0]$, are arrowed green and red, respectively. The inset is the enlarged view of (000) reflection, highlighting its surrounding satellite spots. (c) A typical selected-area electron diffraction (SAED) pattern contains the similar satellite spots. The splitting of these spots indicates two modulations of different wavelength. All satellite spots in (b) were marked, and the corresponding reconstructed inverse FFT image in (d) reveals competition and interpenetration of two types of nano-scale domains, which are indicated by black and red dashed-line rectangles, respectively. The scale bar is 5 nm. (e) Average electron-energy loss spectra (EELS) for the two separated phase regions (black and red dashed-line rectangle regions, respectively) show La inhomogeneity and slight chemical shift of Mn *L*-edge. The slight difference between Mn *L*-edges while obvious difference between La *M*-edges are due to average Mn oxidation states are +3.74 and +3.67 while La/Mn atomic ratios are 0.26 and 0.33 for the two phases, respectively (see main text). Note that shift of Mn *L*-edge towards lower energy indicates lower oxidation states. Two regions also reveal different modulated periodicities, as analyzed in Figure 2 and Figure 3, respectively.

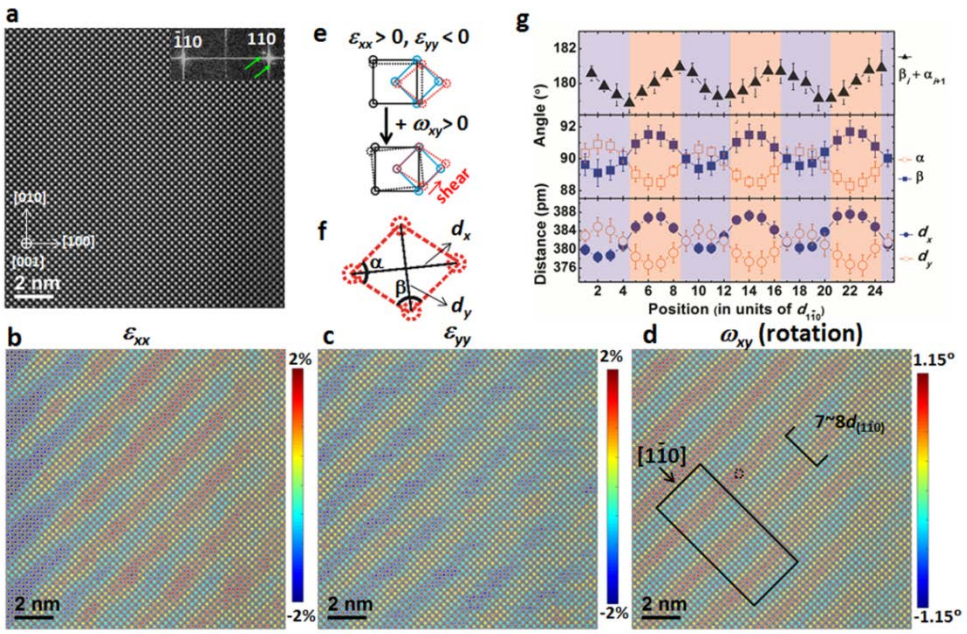

Figure 2. Local picometer precision strain maps (PPSM) from a nanoscale phase with unidirectional modulation in a LSMO-0.7 crystal. (a) An atomic-resolution HAADF image along the [001] zone axis. The inset is the enlarged view of the (110) and ($\bar{1}$10) main Bragg reflections from its FFT pattern. Two satellite spots neighboring (110) with modulation vector $\boldsymbol{q}_1 = 0.131(\boldsymbol{a}^* - \mathbf{b}^*)$, corresponding to 7~8 modulated periodicity along [1$\bar{1}$0], are marked by green arrows. Real-space strain analysis for (a) with uniaxial strain component ε_{xx} and ε_{yy} and rotation ω_{xy} (°) map is shown in (b), (c), and (d), respectively. All the strain is in reference to a perfect square unit cell with side length of 382 pm. The ε_{xx} and ε_{yy} could clearly display uniaxial deformation along [100] (x) and [010] (y), respectively. 7~8 modulated periodicity along [1$\bar{1}$0] is visualized in (d). (e) A schematic of the deformation for the dashed-line square region in (d) (the [001] projection of one body-centered tetragonal unit cell). The black solid-line square and black dashed-line rectangle is one unit cell before and after deformation, respectively. Note that the total strain could also be described by simple shear strain along [110] or [$\bar{1}\bar{1}$0], clearly revealed by the deformation of one primitive cell. The blue solid-line and red dashed-line lozenge is one primitive cell before and after deformation, respectively. (f) Parameters of this primitive cell used to evaluate local strain. α and β are two neighboring inner angles, and d_x and d_y is diagonal line along x ([100]) and y ([010]), respectively. (g) α and β angles, and d_x and d_y distances in each primitive cell along [1$\bar{1}$0] for the rectangle region in (d). The sum of α_{i+1} and β_i for two neighboring primitive cells is also plotted to better reflect 180° reversal of the simple shear strain from along [110] to [$\bar{1}\bar{1}$0], corresponding to alternating red and blue stripes in (b), (c) and (d).

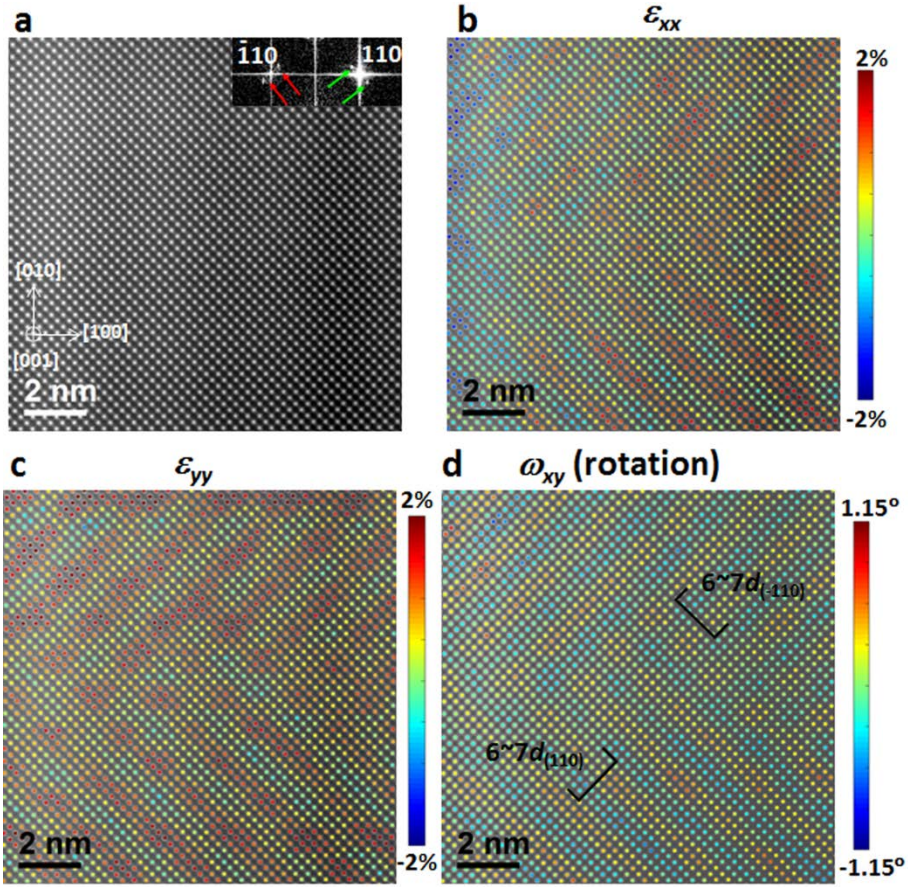

Figure 3. Local picometer precision strain maps (PPSM) in 90° nanoscale domains with bidirectional modulations in LSMO-0.7 single crystal. (a) An atomic-resolution HAADF image along the [001] zone axis for for a 90° domain region. The inset is the enlarged view of the (110) and ($\bar{1}$10) main Bragg reflections from its FFT pattern. Two sets of satellite spots neighboring (110) and ($\bar{1}$10) are marked by green and red arrows, respectively. The modulation vector for them are $\boldsymbol{q}_1 = 0.157(\boldsymbol{a}^* - \mathbf{b}^*)$ and $\boldsymbol{q}_2 = 0.157(\boldsymbol{a}^* + \mathbf{b}^*)$, corresponding to 6~7 modulated periodicity along [1$\bar{1}$0] and [110], respectively. Real-space strain analysis for (a) with uniaxial strain component ε_{xx} and ε_{yy} and rotation ω_{xy} (°) map is shown in (b), (c), and (d), respectively. Similar to Figure 2e, the total strain for the two domains could be described by simple shear strain along [110] (or [$\bar{1}\bar{1}$0]) and [1$\bar{1}$0] (or [$\bar{1}$10]), respectively.

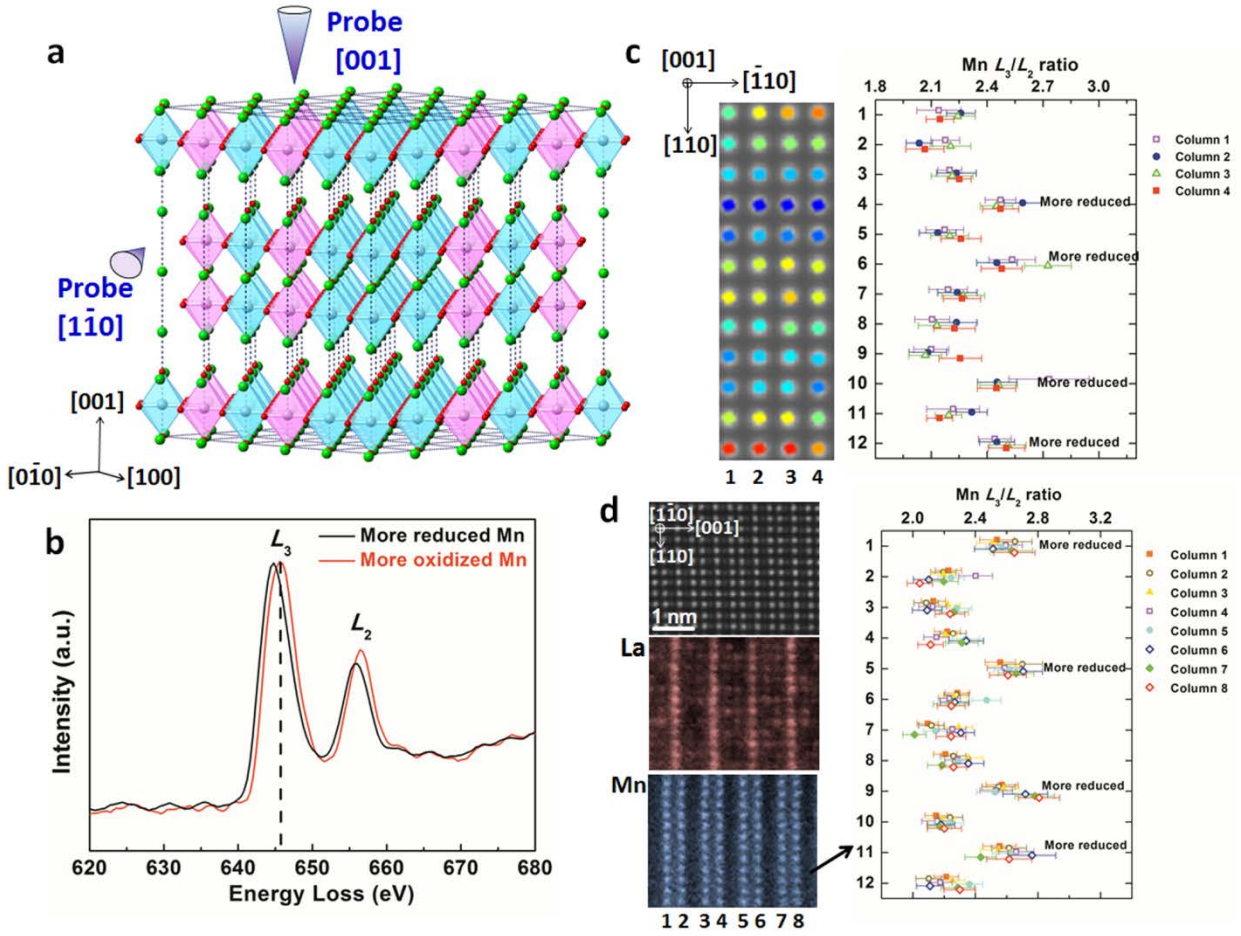

Figure 4. Charge ordering stripes in (110) correlated with PPSM evidenced by atomic-scale EELS mapping. (a) A schematic for the EELS scanning respectively along the direction of [001] and [1$\bar{1}$0], both in (110) plane. Mn^{3+} ions reside in pink O octahedra while Mn^{4+} ions are in blue O octahedra. (b) Comparison between EEL spectra from columns involving Mn cations with more reduced and more oxidized states. Note that Mn with more reduced states shows larger $L_{2,3}$ ratio, and chemical shift towards lower energy. (c) The left panel is strain distribution in a [001] projected HAADF image for EELS mapping region, and the colors represent the levels of positive and negative strain as in Figure 2. The right panel reveals the corresponding Mn $L_{2,3}$ intensity ratios for 4 columns of atomic columns in the left panel. (d) The left panel shows a [1$\bar{1}$0] projected HAADF image, and its corresponding La $M_{4,5}$ and Mn $L_{2,3}$ maps. The right panel gives the Mn $L_{2,3}$ intensity ratios for 8 columns of atomic columns in the Mn $L_{2,3}$ map. Note the combination of (c) and (d) indicates the formation of charge ordering stripes in the (110) plane.

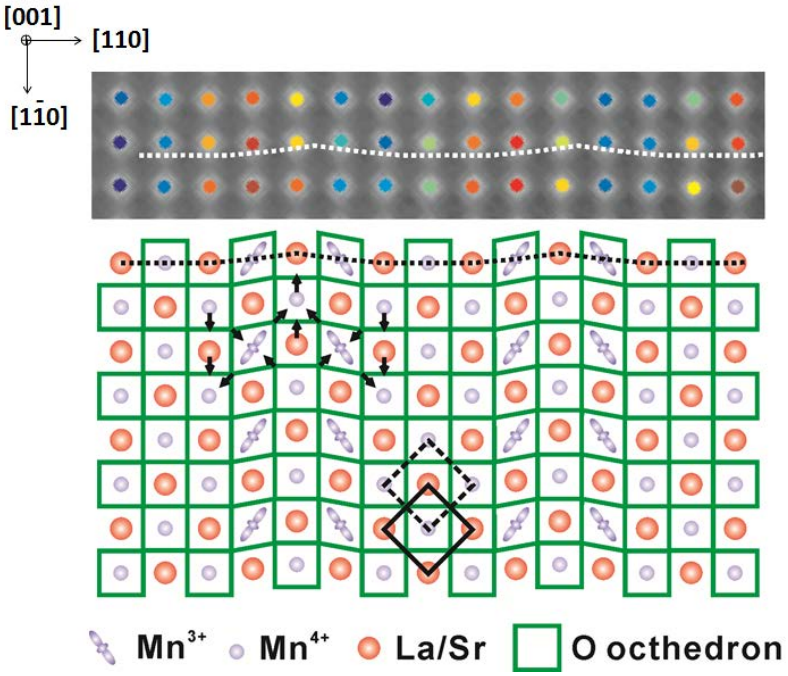

Figure 5. Proposed model of Jahn-Teller distortion accompanied by the cooperative displacements of La/Sr and Mn^{4+} and local PPSM. Note that this schematic only displays charge ordering along [110] with periodicity of $6d_{(110)}$ and the Jahn-Teller distortion in one layer of the structure, as on unit cell marked by the black solid-line square. Another layer shifts ½[1$\bar{1}$0], as revealed by the black dashed-line square. In the projection of [001], La/Sr and Mn in neighboring layers overlap, while the displacements of them are towards the same direction. The displacements induced transverse simple shear map is shown on the top, and the colors represent the levels of positive and negative strain as in Figure 2. The 180° strain reversal occurs between the Mn^{3+} stripes as revealed by the white and black dashed lines, consistent with the variation of sum inner angles between two neighboring primitive cells in Figure 2g.
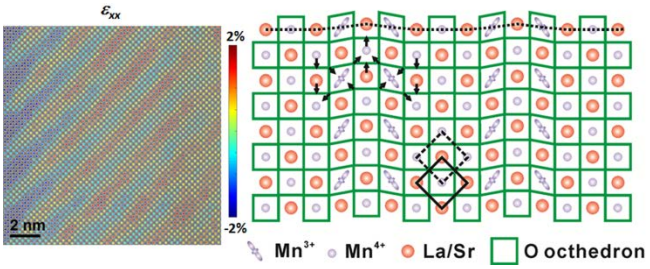
TOC graphic